Frontiers of Information Technology & Electronic Engineering
www.jzus.zju.edu.cn; engineering.cae.cn; www.springerlink.com
ISSN 2095-9184 (print); ISSN 2095-9230 (online)
E-mail: jzus@zju.edu.cn

Port and radiation pattern decoupled metasurface-loaded patch antenna using deep-learning-assisted optimization for MIMO applications*

Gu LIU[1], Jiajiang SHEN[1], Lei MA[1], Wei QIN[1], Wenwen YANG[†‡1], Lei GUO[2], Jianxin CHEN[1]

[1]*School of Information Science and Technology, Nantong University, Nantong 226019, China*

[2]*School of Information and Communication Engineering, Dalian University of Technology, Dalian 116024, China*

[†]E-mail: wwyang2008@hotmail.com

Received Feb. 25, 2025; Revision accepted June 20, 2025; Crosschecked Sept. 15, 2025

Abstract: A metasurface-loaded 1×2 patch array antenna assisted by a deep-learning optimization method is proposed to realize port and radiation pattern decoupling simultaneously to enhance the isolation among elements in multi-input multi-output (MIMO) systems. The deep-learning-assisted optimization method uses an artificial neural network (ANN) and a particle swarm optimization (PSO) algorithm to seek the optimal structure of the antenna to achieve port decoupling with undistorted radiation patterns. The ANN is trained to describe the nonlinear relationship between the geometric parameters and the responses of the antenna. The PSO algorithm, guided by the cost function and number of iterations, is used to optimize the structure of the antenna according to the cost function combined with the trained ANN. Finally, by constraining the cost function, we obtain a 1×2 patch array antenna with a metasurface fixed above by studs, which achieves port and radiation pattern decoupling simultaneously. To validate the principle and design method, we designed, fabricated, and measured an antenna prototype with dimensions of $0.88\lambda_0\times0.47\lambda_0\times0.21\lambda_0$ (λ_0 is the wavelength in free space at the center frequency). The measured fractional bandwidth is 8% (4.8–5.2 GHz). The isolation of the two-element patch antenna increases from 7.6 dB to 24.3 dB with an envelope correlation coefficient (ECC) of <0.0005 at $0.35\lambda_0$. Moreover, the H-plane radiation pattern of each element is consistent and symmetric in the broadside direction. These characteristics make the proposed antenna suitable for MIMO antenna systems with close spacing.

Key words: Artificial neural network (ANN); Particle swarm optimization (PSO) algorithm; Mutual coupling; Radiation pattern restoration; Metasurface

https://doi.org/10.1631/FITEE.2500119 **CLC number:** TN82

1 Introduction

Multi-input multi-output (MIMO) array antennas (Alibakhshikenari et al., 2018, 2019a, 2019b, 2020a, 2020b, 2020c; Abbasi et al., 2025) have been widely used in wireless communication devices, such as base stations (Alibakhshikenari et al., 2018, 2019b; Abbasi et al., 2025), benefiting from their advantages of a large channel capacity and wide beam coverage range (Alibakhshikenari et al., 2020a, 2020b, 2020c). However, with reduced antenna spacing, increased mutual coupling between antennas may lead to deterioration of port isolation. Moreover, the radiation pattern of antenna elements may worsen, which decreases the performance of beamforming (Chen et al., 2008; Alibakhshikenari et al., 2021, 2024; Bouknia et al., 2021). Therefore, it is well worth designing a MIMO

‡ Corresponding author

* Project supported by the National Natural Science Foundation of China (Nos. 62071256 and 62071263)

ORCID: Gu LIU, https://orcid.org/0009-0001-5419-0060; Wenwen YANG, https://orcid.org/0000-0002-0492-5508

array antenna that can realize port and radiation pattern decoupling simultaneously.

Many reported decoupling designs have achieved significant achievements in improving decoupling performance. These designs are based on two main methods. The first involves adding a structure between the antenna elements, such as a neutralization line (Gao et al., 2020; Femenias and Riera-Palou, 2022; Din et al., 2023), a defected ground structure (DGS) (Huang et al., 2023; Han and Hong, 2024; Heo et al., 2024), an electromagnetic band gap (EBG) (Kennedy and Eberhart, 1995; Jensen and Wallace, 2004; Hussein et al., 2024; Khan et al., 2025), and a metal decoupling structure (Li et al., 2022; Lai et al., 2023; Kiani et al., 2024), to introduce an extra decoupling path to counteract the original coupling. However, the radiation pattern of the elements is usually destroyed because the extra structure is so close. The second approach is self-decoupling, which involves using the inherent characteristics of the antenna rather than extra decoupling structures (Paulraj et al., 2004; Poli et al., 2007; Lin et al., 2020; Liu F et al., 2020; Liu RP et al., 2020; Madani et al., 2021; Ma et al., 2023; Odabasi et al., 2023; Liu GY et al., 2024a, 2024b; Mondal et al., 2024; Ozer et al., 2024). A weak electric field can be obtained in the coupled element through field cancellation. Therefore, the coupling between elements can be significantly reduced without extra structures. However, antenna elements usually need to have specific shapes or spacings to achieve a weak electric field.

In recent years, metasurfaces (Sun et al., 2021; Shi et al., 2022; Tong et al., 2022a, 2022b, 2024; Wang ZB et al., 2023; Qi et al., 2024; Qian et al., 2024; Wang MN et al., 2024) composed of planar subwavelength scattering units have been gradually applied to antenna decoupling (Xia et al., 2015; Wu et al., 2023; Xiao et al., 2024; Xiong et al., 2024; Xu et al., 2024; Zhai et al., 2024) due to their flexible design and lack of restrictions on radiators. Two pairs of double-sided parallel strips were introduced as bandstop filters to separate the propagation of electromagnetic (EM) waves to the coupled patch (Wu et al., 2023). Square rings (Xia et al., 2015) and hexagon rings (Xiao et al., 2024) were used to control the amplitude and phase of radiation waves, which can counteract directly coupled waves. A unit cell composed of four L-shaped strips and a rectangular patch (Xiong et al., 2024) was proposed for reflecting the radiated waves to cancel the directly coupled EM waves, and a 6-dB port isolation enhancement was obtained. A metasurface composed of uniform array metal patches was presented as an EBG structure to block surface waves (Xu et al., 2024). A metasurface proposed by Zhai et al. (2024) was composed of five square loops to improve the coupling of elements from 21 dB to 27 dB. However, these designs can realize port decoupling but not radiation pattern decoupling because of the complexity of the numerical calculations.

In this paper, a metasurface-loaded patch antenna designed by a deep-learning-assisted optimization method is proposed to realize port and radiation pattern decoupling simultaneously. Complex theoretical analysis can be avoided owing to the application of a deep-learning-assisted optimization method composed of an artificial neural network (ANN) model and a particle swarm optimization (PSO) algorithm. The ANN is trained to build the nonlinear relationship between the geometric parameters and the EM response of the desired antenna. The PSO algorithm is used with the trained ANN to optimize the structure of the antenna with the constraint of a cost function. The proposed antenna can improve port isolation from 7.6 dB to 24.3 dB, and the H-plane radiation pattern of the element can maintain symmetry in the broadside direction.

2 Antenna design

2.1 Antenna structure

Fig. 1 shows the configuration of the proposed metasurface-loaded decoupled patch antenna. The top layer is located on the upper surface of the substrate named Sub 1, which includes 18 (6×3) periodic unit cells. For clarity, a unit cell has been enlarged in Fig. 1b. The unit cell is composed of 64 (8×8) pixel patches and can be represented by a binary 8×8 matrix $\boldsymbol{T}$, where "0" is the vacuum and "1" stands for the metal. The middle layer is printed on the upper surface of the substrate named Sub 2 and comprises two patches excited by the SubMiniature version A (SMA) connector. Sub 1 and Sub 2 are RO5880 substrates with relative permittivity ε_r=2.2 and loss tangent tanδ= 0.0009. The gap between Sub 1 and Sub 2 (G) was chosen as 10 mm, as in Xiao et al. (2024).

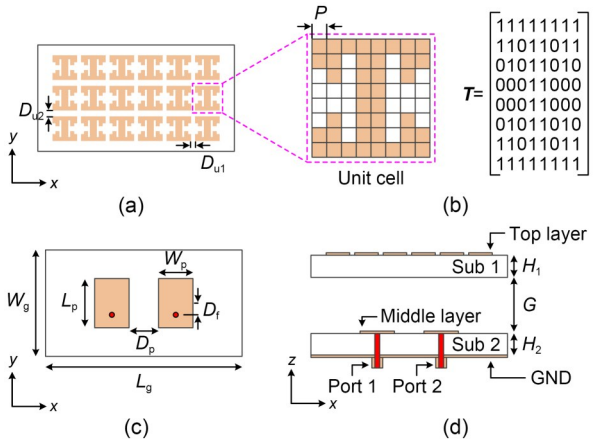

Fig. 1 Configuration of the proposed metasurface-loaded decoupled patch antenna: (a) top layer; (b) enlarged view of the unit cell; (c) middle layer; (d) side view. L_g=90, W_g=50, L_p=19.2, W_p=18, D_p=3, D_f=4, D_{u1}=1, D_{u2}=2, P=1, G=10, H_1=1.57, and H_2=0.787 (unit: mm)

2.2 Mechanism of port and radiation pattern decoupling with metasurface loading

Fig. 2 depicts the mechanism by which the metasurface realizes antenna decoupling. Element 1 is excited, and element 2 is loaded with a matching load. The introduction of the metasurface placed above the array antenna adds an extra coupled path (Path 2) between the antenna elements, which is superimposed with the surface coupled wave generated by the original coupled path (Path 1) through the gap between the two elements. Port decoupling can be achieved when the field generated by the superimposed waves near the feeding port of the coupled element is a weak field.

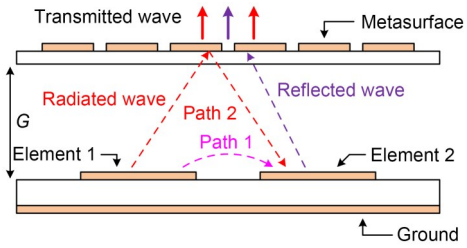

Fig. 2 Schematic diagram of coupling paths of a metasurface-loaded two-element patch antenna

Radiation pattern decoupling can be achieved if the EM waves coupled to element 2 via the two above paths completely cancel out. Unfortunately, it is almost impossible to calculate the required amplitudes and phases for port and radiation pattern decoupling through theoretical analysis because the coupled element is a two-dimensional structure rather than a point. Hence, in this design, an ANN is used for directly predicting the responses of the metasurface-loaded patch antenna, avoiding complex numerical calculations and time-consuming parameter tuning.

2.3 Building an ANN to predict the EM response of a metasurface-loaded patch antenna

Fig. 3 shows the topology of the ANN with one input layer, five hidden layers, and one output layer. In this ANN, five hidden layers with 50, 100, 150, 300, and 600 neurons are used to connect the input and output layers to achieve accurate result prediction. The input layer represented by matrix $\boldsymbol{S}$ comprises the structural parameters of the antenna. The output

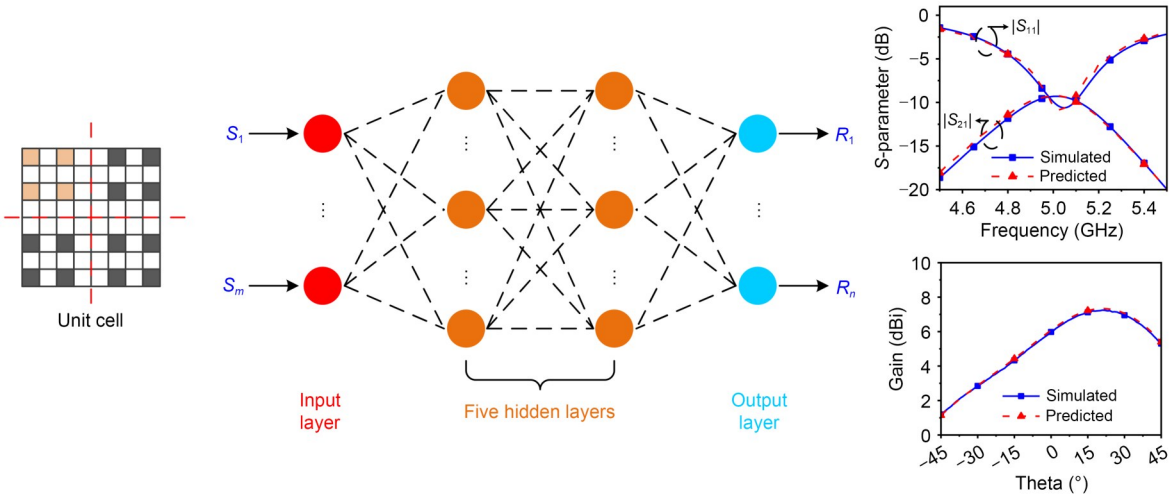

Fig. 3 Topology of an ANN with one input layer, five hidden layers, and one output layer

layer represented by matrix $\boldsymbol{R}$ comprises the EM responses of the antenna, such as the S-parameter and the gain of the antenna.

To accurately express the structural characteristics of the proposed antenna, the input layer has 18 neurons. Sixteen neurons are used to load the structural characteristics of the metasurface, represented by a 4×4 matrix $\boldsymbol{t}_c$, and the other two neurons are the length of the patch (L_p) and the location of the SMA (D_f), considering the EM perturbation of the metasurface on the patch antenna to enhance control over the impact of the parameters of the antenna on its response.

Fig. 4 shows the design process of representing the structural features of the metasurface with a 4×4 matrix $\boldsymbol{t}_c$. First, the design space is a 53 mm×28 mm printed circuit board (PCB) divided into 18 (6×3) identical unit cells (Fig. 4a), and a 1-mm interval and a 2-mm interval are set between adjacent unit cells along the x-axis and y-axis, respectively, to separate each unit cell. Second, Fig. 4b shows that each unit cell is divided into 8×8 pixels by a square with a side length of 1 mm. The structure of each pixel can be represented using two discrete values to indicate whether it covers a metal or not, where a value of "1" means a piece of metal, and a value of "0" stands for a void. Finally, the unit cell has an axisymmetric distribution around the center for the symmetric radiation pattern. Hence, the structural features of the designed metasurface can be described by its left-upper part, which can be represented by a 4×4 matrix $\boldsymbol{t}_c$. As an example, the shape of the unit cell shown in Fig. 4b can be described as a 4×4 matrix $\boldsymbol{t}_c$ (Fig. 4c).

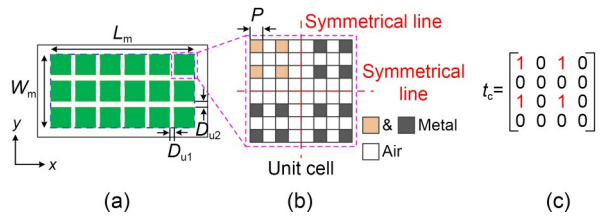

Fig. 4 Schematic of the metasurface: (a) the unit cell distribution of the metasurface; (b) the pixelated distribution of each unit cell; (c) the 4×4 matrix describing the shape of (b). L_m=53, W_m=26, D_{u1}=1, D_{u2}=2, and P=1 (unit: mm)

The output layer includes 563 neurons, which represent $|S_{11}|$ and $|S_{21}|$ of the 101 frequency points ranging from 4.5 GHz to 5.5 GHz to ensure the accurate prediction of the antenna performance, with 0.01-GHz steps, and the H-plane radiation pattern ranges from −180° to 180° with 1° intervals at 5 GHz. The results of the output layer can be obtained by simulation using computer simulation technology (CST) software.

It is necessary to build a diverse and accurate dataset for achieving effective training of the ANN and accurate prediction of the performance of the antenna. In this design, a dataset containing 6000 sets of 4×4-0/1 matrix, L_p, and D_f at random, which consumes about 180 h for simulation, is used to train the ANN, and the corresponding results are normalized to between 0 and 1. The activation function of each layer is the leaky rectified linear unit (Leaky ReLU) function and the optimizer is adaptive moment estimation (Adam). The learning rate is determined to be 0.001. The mean square error (MSE) used to assess the performance of the ANN is given by

$$\mathrm{MSE}=\frac{\sum_{i=1}^{N}(y_i-y_i^*)^2}{N}, \tag{1}$$

where y_i is the simulated results of the dataset, y_i^* represents the results predicted by the ANN, and N is the total number of samples used to train the ANN (6000). L1 regularization and a dropout mechanism were used to constrain the weights of neurons and decrease reliance on specific neurons. All calculations were carried out by an Intel i7-12700KF 3.6-GHz machine with 64 GB RAM. Fig. 5 shows the MSE loss changing with each epoch. As the number of epochs increases, the MSE loss converges to 0.003.

Once the ANN is well trained, $\boldsymbol{R}$ can be obtained if $\boldsymbol{S}$ is determined. Fig. 6 illustrates a comparison using two validated samples between $\boldsymbol{R}$ values predicted by the ANN and those simulated by CST. The predicted and simulated results are highly consistent.

2.4 Combining the PSO algorithm to realize the port and radiation pattern decoupling

The PSO algorithm (Zhang and Pedersen, 2016; Zhao et al., 2024) is applied to realize the port and radiation pattern decoupling after the training of the ANN, as shown in Fig. 7. The optimized input can be

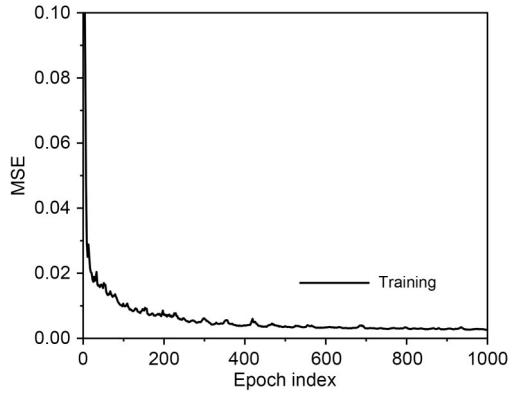

Fig. 5 MSE results during the training process

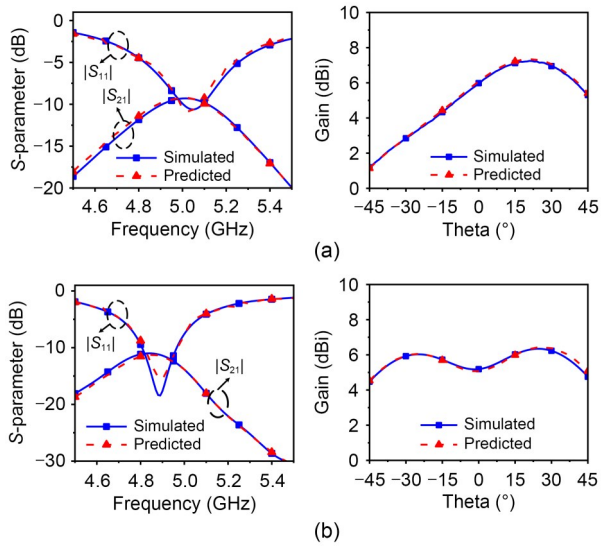

Fig. 6 Simulated and predicted *S*-parameters and H-plane radiation patterns of two validated samples: (a) sample 1; (b) sample 2

searched for by updating the velocity and position of the particle. The purpose of the PSO algorithm is to construct the cost function, which can be calculated by the output of the trained ANN. The cost function is given by

$$C=w(s_{11}-m)+w(s_{21}-n)+(1-2w)\sum_{k=0}^{45}\left|s_{(k)}-s_{(-k)}\right|, \quad (2)$$

where s_{11} is $|S_{11}|$ at 5 GHz, s_{21} is $|S_{21}|$ at 5 GHz, and $s_{(k)}$ and $s_{(-k)}$ are the gains of the H-plane beam at degrees k and $-k$, respectively, which are predicted from the trained ANN. Moreover, m and n are the desired responses, which are set as −20 and −25, respectively.

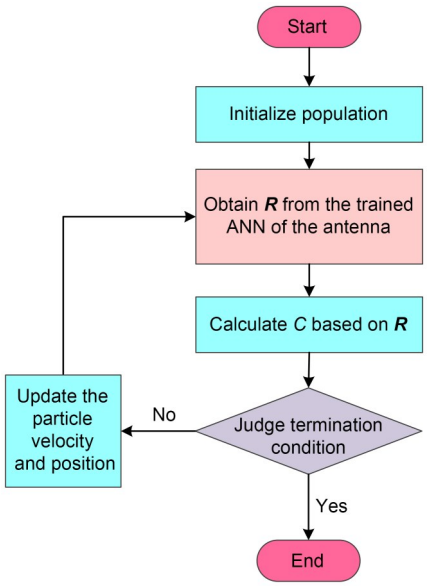

Fig. 7 PSO algorithm flowchart for optimization of the metasurface-loaded patch antenna

The weight of the port matching and isolation (w), whose value is 0.1, is used to improve the importance of radiation pattern optimization. The minimum value of the cost function calculated by ***R*** generated by the trained ANN model is searched for until the PSO algorithm stops running. Finally, a group of parameters is found by the proposed method (Table 1), which consumes 468 s. The simulated results and the results calculated by the proposed method are compared in Fig. 8, which shows that the simulated results are in good agreement with the predicted results of the optimized antenna. Furthermore, compared with the optimized antenna without the metasurface loading, the proposed antenna decreases the mutual coupling from −7.6 dB to −24.3 dB, and the H-plane radiation pattern is corrected to be symmetrical about the broadside direction.

Table 1 Optimized input based on the PSO

L_p (mm)	D_f (mm)	Pixel encoding of the metasurface	Time cost (s)
19.2	4	[1111110101010001]	468

Fig. 9 shows the change in the average electric field amplitude of the patch antenna with and without metasurface loading. As shown in Fig. 9a, the electric field in the coupled patch is strong without metasurface

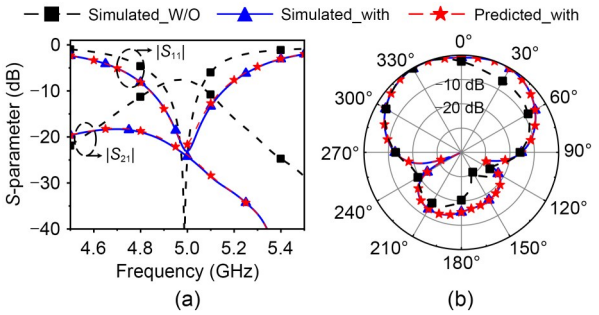

Fig. 8 Predicted results of the optimized input (Predicted_with), simulated results of the optimized input (Simulated_with), and simulated results of the optimized antenna without the metasurface loading (Simulated_W/O): (a) *S*-parameter; (b) normalized H-plane radiation pattern

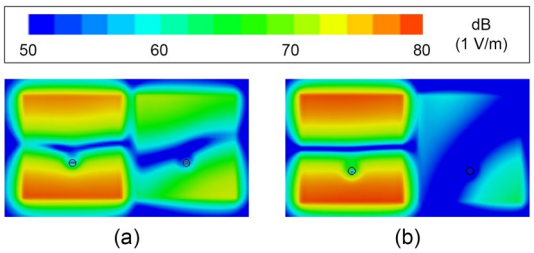

Fig. 9 Average electric field amplitude of the 1×2 patch antenna: (a) without metasurface loading; (b) with metasurface loading. References to color refer to the online version of this figure

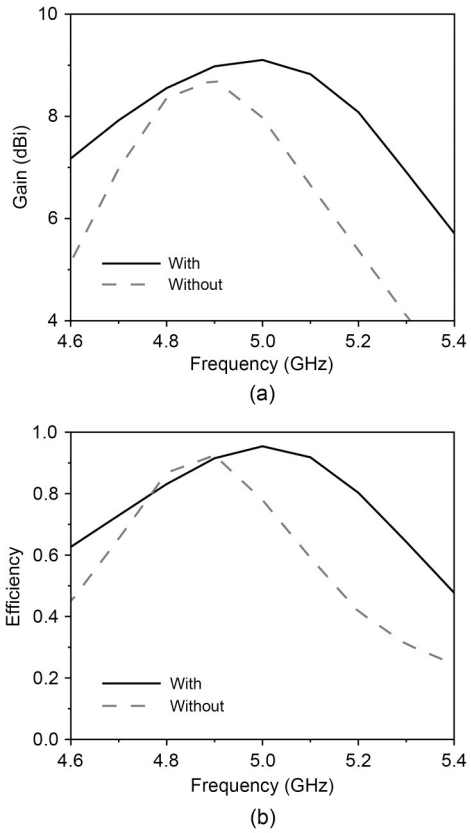

Fig. 10 Gain (a) and efficiency (b) of the 1×2 patch antenna with a loaded metasurface

loading, which shows that there is strong coupling between the two patches. Furthermore, with metasurface loading, the electric field in the coupled patch becomes weak, which proves that the EM waves via Path 2 partly counteract those through Path 1 (Fig. 2).

To demonstrate the advantages of the metasurface-loaded patch antenna array, Fig. 10 shows the gain and efficiency of the 1×2 patch antenna with a loaded metasurface, with two elements excited with the same amplitude and phase. The gain increases from 8 dBi (without) to 9.1 dBi (with) at 5 GHz, and the efficiency correspondingly increases from 77.9% to 95.4%.

For investigating the decoupling performance of the proposed metasurface under large arrays, Fig. 11 shows a 1×4 metasurface-loaded element array optimized by the machine learning method. The *S*-parameter and H-plane radiation pattern at 5 GHz are shown in Fig. 12. The isolation increases from 8.65 dB to 16.30 dB, and the radiation pattern is restored to broadside.

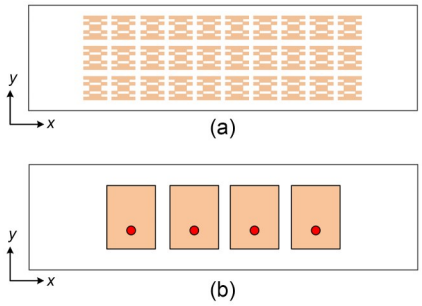

Fig. 11 Structure diagram of the 1×4 element array loaded on the metasurface: (a) metasurface; (b) 1×4 patch antenna

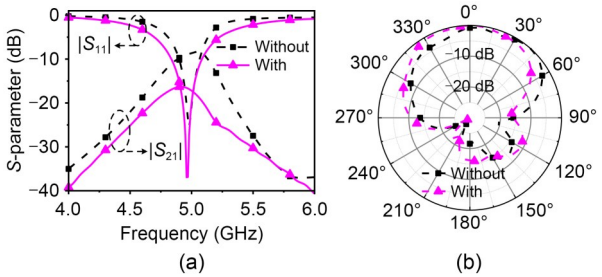

Fig. 12 *S*-parameter (a) and radiation pattern (b) of the 1×4 element array

3 Results

A prototype of a 1×2 metasurface-loaded patch antenna was finally designed, fabricated, and measured with Keysight E5230C for the *S*-parameters and an anechoic chamber for gain and radiation patterns (Fig. 13). Fig. 14 shows that the simulated and measured *S*-parameters agreed well with each other. The measured 10-dB impedance matching bandwidth is 0.4 GHz (4.8–5.2 GHz), or the fractional bandwidth is 8%. The mutual coupling level of the proposed antenna is −24.3 dB at 5 GHz.

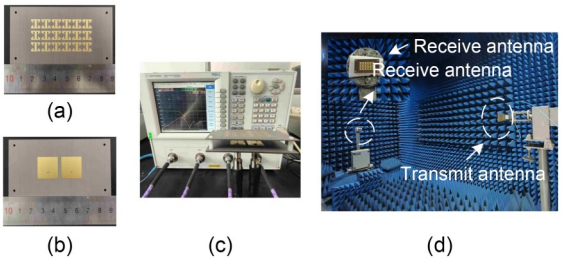

Fig. 13 Photographs of the fabricated metasurface-loaded patch antenna and the measured environment: (a) metasurface; (b) two-element patch antenna; (c) Keysight E5230C; (d) anechoic chamber

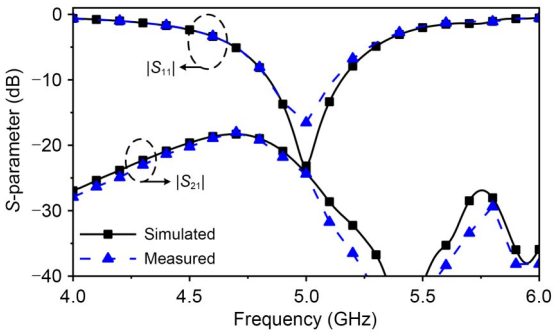

Fig. 14 Simulated and measured *S*-parameters of the proposed antenna

Fig. 15 shows that the simulated and measured gain, total efficiency, and envelope correlation coefficient (ECC) of the prototype are in good agreement with each other. The peak gain is 6.13 dBi. The total efficiency and the ECC are higher than 90% and lower than 0.0005, respectively. Compared with the traditional 1×2 patch antenna without the metasurface, the maximum ECC across the frequency band is reduced from 0.3 to 0.00006, which shows that the proposed antenna array has good radiation and diverse performance.

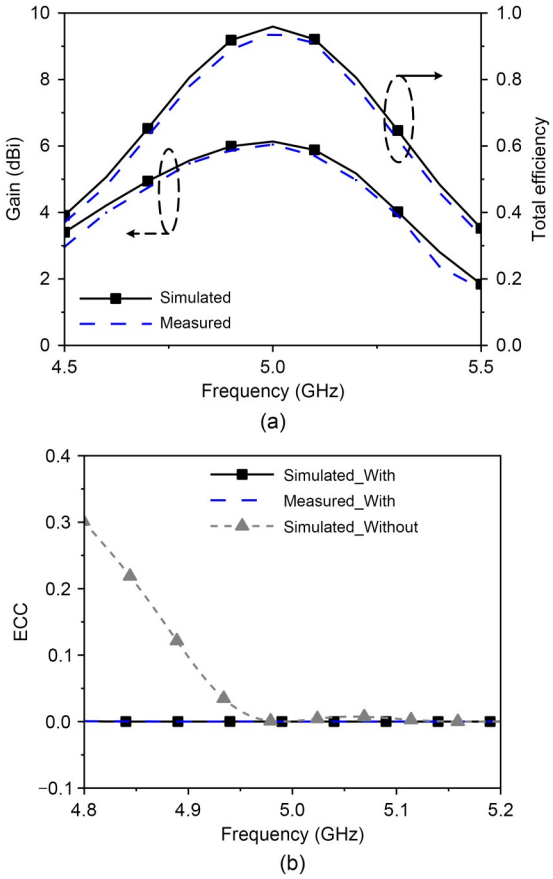

Fig. 15 Simulated and measured gain and total efficiency (a) and ECC (b) of the proposed patch antenna

Fig. 16 shows the simulated and measured radiation patterns of the proposed metasurface-loaded antenna array for ports 1 and 2 at 5 GHz. Figs. 16b and 16d show that the H-plane radiation patterns for ports 1 and 2 exhibited great symmetry in the broadside direction. The cross-polarization levels in the E-plane and H-plane for port 1 and port 2 are both below −18 dB.

Fig. 17 shows the trends of the calculated channel capacity (CC) and bit error rate (BER) of the proposed antenna with a signal-to-noise ratio (SNR) at 5 GHz. The black dashed line in Fig. 17 represents the proposed antenna without the metasurface, and the blue solid line represents it with the metasurface. The CC is upgraded and the BER is reduced after loading the metasurface at any SNR (Zhao et al., 2024).

Table 2 summarizes the performance of the proposed antenna and previously reported designs. Compared with port decoupled antennas (Jensen and Wallace, 2004; Xia et al., 2015; Li et al., 2022; Huang et al., 2023; Wu et al., 2023; Xiao et al., 2024; Xiong et al.,

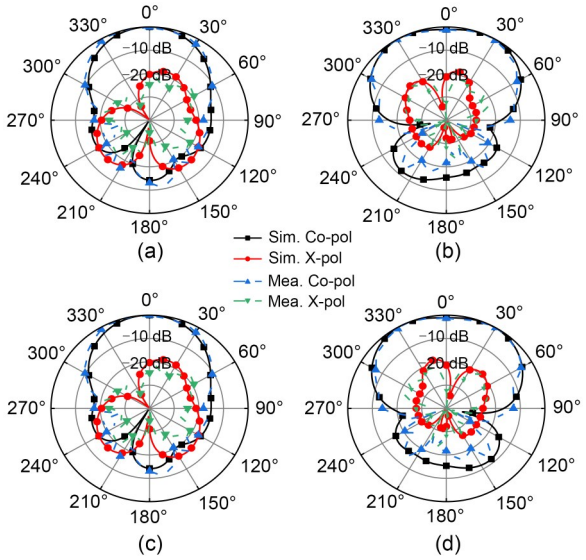

Fig. 16 Simulated and measured radiation patterns of the proposed antenna at 5 GHz for two ports: (a) E-plane of port 1; (b) H-plane of port 1; (c) E-plane of port 2; (d) H-plane of port 2

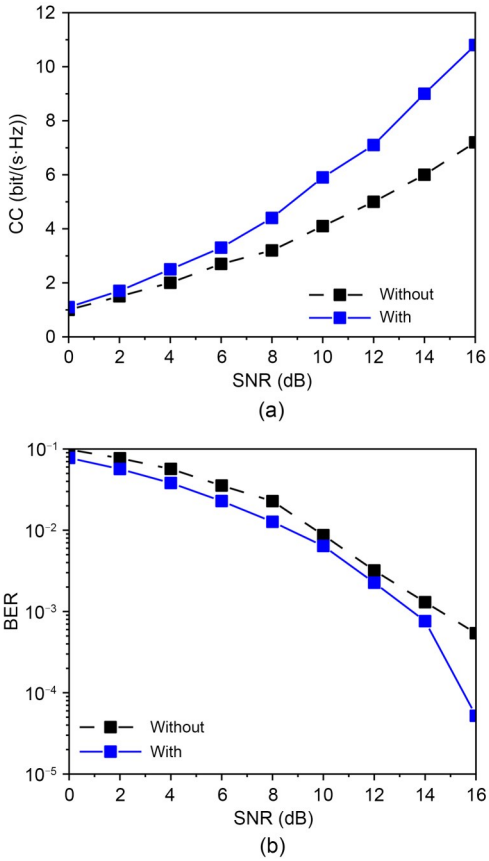

Fig. 17 Channel capacity (a) and bit error rate (b) for the proposed antenna before and after loading the metasurface at 5 GHz. References to color refer to the online version of this figure

2024), the proposed metasurface-loaded decoupled antenna achieves radiation pattern coupling and substantial port isolation improvement. Compared with self-decoupled antennas (Paulraj et al., 2004; Liu F et al., 2020; Ma et al., 2023), our proposed antenna can realize port and radiation pattern decoupling simultaneously with the minimum center-to-center spacing

Table 2 Performance summary of the proposed and state-of-the-art designs

Reference	Frequency band (GHz)	Size ($\lambda_0\times\lambda_0\times\lambda_0$)	Decoupling method	C-C/E-E spacing (λ_0)	BW (%)	MCLR (dB)	PG (dBi)	PE (%)	RPD	Design complexity
Huang et al., 2023	11.05–13.06	0.52×0.22×0.25	DGS	0.29/0.07	16.7	15	4.9	N.A.	No	Complex
Jensen and Wallace, 2004	25.3–30.6	0.89×0.44×0.14	EBG	0.44/0	19	15	5	90	No	Complex
Li et al., 2022	3.28–3.6	0.74×0.32×0.036	Metal decoupling structure	0.5/0.25	9.3	15	5.34	87	No	Medium
Liu F et al., 2020	2.394–2.53	0.46×0.42×0.008	Self-decoupling	0.44/0.02	5.5	10	8	92	Yes	Easy
Ma et al., 2023	2.38–2.52	0.83×0.42×0.056	Self-decoupling	0.42/0	5.7	11	8.8	86	Yes	Medium
Paulraj et al., 2004	4.82–5.08	2.17×1.53×0.05	Self-decoupling	0.6/0.05	5.3	8	6	94	Yes	Complex
Wu et al., 2023	2.5–2.7 3.4–3.6	0.87×0.52×0.15	Metasurface	0.35/0.01	7.7/ 5.7	10	8.6	88	No	Complex
Xia et al., 2015	24.11–29.68	0.82×0.39×0.36	Metasurface	0.4/0.05	20.7	17	9	95	No	Complex
Xiao et al., 2024	5.13–5.26	1.21×0.89×0.21	Metasurface	0.36/0.03	2.5	17.3	10	N.A.	No	Medium
Xiong et al., 2024	26.18–30.34	0.98×0.49×0.18	Metasurface	0.49/0.35	14.7	6	5	N.A.	No	Complex
This work	4.8–5.2	0.88×0.47×0.21	Metasurface	0.35/0.05	8	16.7	6.13	96	Yes	Easy

C-C: center-to-center; E-E: edge-to-edge; BW: bandwidth; MCLR: mutual coupling level reduction; PG: peak gain; PE: peak efficiency; RPD: radiation pattern decoupling; N.A.: not available

and wider bandwidth. Meanwhile, simultaneous decoupling can be realized with easy design, and the design process avoids complex theoretical analysis and time-consuming parameter optimization.

4 Conclusions

In this paper, we present a metasurface-loaded port and radiation pattern decoupled patch antenna designed by deep-learning-assisted optimization. First, the nonlinear relationship between the geometric parameters and the EM responses of the antenna can be built by the trained ANN model, saving much simulation time when obtaining extra EM responses based on different geometric parameters. Second, intelligent geometric parameter optimization can be realized by combining the PSO algorithm and the trained ANN. Finally, by constraining the cost function of the PSO algorithm, the optimized geometric parameters can be obtained for port and radiation pattern decoupling. Results show that the proposed antenna can realize 10-dB impedance matching bandwidth from 4.8 to 5.2 GHz with a 16.7-dB isolation improvement. The total efficiency is higher than 90% and the ECC is lower than 0.0005, which shows that the proposed antenna array has good radiation and diversity performance. Furthermore, the H-plane radiation pattern for each port shows great consistency. Compared with the current metasurface-loaded patch antennas, the proposed antenna can realize a conserved radiation pattern with great port isolation. In addition, the design process is not constrained by complex theoretical analysis. The proposed design concept is an attractive strategy for patch antenna decoupling.

Contributors

Gu LIU and Jiajiang SHEN designed the research, processed the data, and drafted the paper. Lei MA, Wei QIN, Wenwen YANG, Lei GUO, and Jianxin CHEN helped organize the paper. Gu LIU and Wenwen YANG revised and finalized the paper.

Conflict of interest

All the authors declare that they have no conflict of interest.

Data availability

The data that support the findings of this study are available from the corresponding author upon reasonable request.

References

Abbasi NA, Virdee B, Din IU, et al., 2025. High-isolation array antenna design for 5G mm-wave MIMO applications. *J Infrared Millimeter Terahertz Waves*, 46(1):12. https://doi.org/10.1007/s10762-024-01027-3

Alibakhshikenari M, Virdee BS, Shukla P, et al., 2018. Antenna mutual coupling suppression over wideband using embedded periphery slot for antenna arrays. *Electronics*, 7(9): 198. https://doi.org/10.3390/electronics7090198

Alibakhshikenari M, Khalily M, Virdee BS, et al., 2019a. Mutual coupling suppression between two closely placed microstrip patches using EM-bandgap metamaterial fractal loading. *IEEE Access*, 7:23606-23614. https://doi.org/10.1109/ACCESS.2019.2899326

Alibakhshikenari M, Khalily M, Virdee BS, et al., 2019b. Mutual-coupling isolation using embedded metamaterial EM bandgap decoupling slab for densely packed array antennas. *IEEE Access*, 7:51827-51840. https://doi.org/10.1109/ACCESS.2019.2909950

Alibakhshikenari M, Parchin NO, Virdee BS, et al., 2020a. High performance metasurface-based on-chip antenna for terahertz integrated circuits. 3rd Int Workshop on Mobile Terahertz Systems, p.1-4. https://doi.org/10.1109/IWMTS49292.2020.9166324

Alibakhshikenari M, Virdee BS, See CH, et al., 2020b. Impedance matching network based on metasurfaces (2-D metamaterials) for electrically small antennas. IEEE Int Symp on Antennas and Propagation and North American Radio Science Meeting, p.1953-1954. https://doi.org/10.1109/IEEECONF35879.2020.9330460

Alibakhshikenari M, Virdee BS, See CH, et al., 2020c. Metasurface for controlling polarization of scattered EM waves. 4th Australian Microwave Symp, p.1-2. https://doi.org/10.1109/AMS48904.2020.9059504

Alibakhshikenari M, Virdee BS, Althuwayb AA, et al., 2021. An innovative and simple impedance matching network using stacks of metasurface sheets to suppress the mismatch between antennas and RF front-end transceivers circuits. 15th European Conf on Antennas and Propagation, p.1-4. https://doi.org/10.23919/EuCAP51087.2021.9411395

Alibakhshikenari M, Zidour A, Virdee BS, et al., 2024. Innovative UWB phase shifters using groove gap-waveguide technology inspired by metasurfaces for beamforming networks operating at 100 GHz. IEEE Asia-Pacific Microwave Conf, p.740-742. https://doi.org/10.1109/APMC60911.2024.10867275

Bouknia ML, Zebiri C, Sayad D, et al., 2021. Analysis of the combinatory effect of uniaxial electrical and magnetic anisotropy on the input impedance and mutual coupling of a printed dipole antenna. *IEEE Access*, 9:84910-84921. https://doi.org/10.1109/ACCESS.2021.3085949

Chen SC, Wang YS, Chung SJ, 2008. A decoupling technique for increasing the port isolation between two strongly coupled antennas. *IEEE Trans Antenn Propag*, 56(12):3650-3658. https://doi.org/10.1109/TAP.2008.2005469

Din IU, Alibakhshikenari M, Virdee BS, et al., 2023. High performance antenna system in MIMO configuration for 5G

wireless communications over sub-6 GHz spectrum. *Radio Sci*, 58(10):e2023RS007726. https://doi.org/10.1029/2023RS007726

Femenias G, Riera-Palou F, 2022. Wideband cell-free mmWave massive MIMO-OFDM: beam squint-aware channel covariance-based hybrid beamforming. *IEEE Trans Wirel Commun*, 21(7):4695-4710. https://doi.org/10.1109/TWC.2021.3132414

Gao D, Cao ZX, Fu SD, et al., 2020. A novel slot-array defected ground structure for decoupling microstrip antenna array. *IEEE Trans Antenn Propag*, 68(10):7027-7038. https://doi.org/10.1109/TAP.2020.2992881

Han K, Hong S, 2024. Range-angle decoupling technique using wavelength-dependent beamforming for high-resolution MIMO radar. *IEEE Trans Microw Theory Tech*, 72(7):4269-4277. https://doi.org/10.1109/TMTT.2023.3335160

Heo JM, Kim H, Kim DY, et al., 2024. Dual-band dual-polarization decoupling metasurface using stacked mushroom structure with asymmetric via posts. *IEEE Antenn Wirel Propag Lett*, 23(6):1685-1689. https://doi.org/10.1109/LAWP.2024.3366593

Huang H, Yang XS, Wang BZ, 2023. Machine-learning-based generative optimization method and its application to an antenna decoupling design. *IEEE Trans Antenn Propag*, 71(7):6243-6248. https://doi.org/10.1109/TAP.2023.3270716

Hussein H, Elmunim NA, Atasoy F, et al., 2024. A novel MIMO antenna integrated with a solar panel and employing AI-equalization for 5G wireless communication networks. *IEEE Access*, 12:114382-114393. https://doi.org/10.1109/ACCESS.2024.3441830

Jensen MA, Wallace JW, 2004. A review of antennas and propagation for MIMO wireless communications. *IEEE Trans Antenn Propag*, 52(11):2810-2824. https://doi.org/10.1109/TAP.2004.835272

Kennedy J, Eberhart R, 1995. Particle swarm optimization. Proc Int Conf on Neural Networks, p.1942-1948. https://doi.org/10.1109/ICNN.1995.488968

Khan I, Song CY, Ullah H, et al., 2025. A novel multiband low mutual coupling quad-element MIMO antenna for advanced communication systems. *IEEE Access*, 13:65198-65215. https://doi.org/10.1109/ACCESS.2025.3558518

Kiani SH, Munir ME, Savci HŞ, et al., 2024. Dual-polarized wideband 5G N77 band slotted MIMO antenna system for next-generation smartphones. *IEEE Access*, 12:34467-34476. https://doi.org/10.1109/ACCESS.2024.3370860

Lai QX, Pan YM, Zheng SY, 2023. A self-decoupling method for MIMO antenna array using characteristic mode of ground plane. *IEEE Trans Antenn Propag*, 71(3):2126-2135. https://doi.org/10.1109/TAP.2023.3240561

Li JK, Zhai HQ, Zhao LY, et al., 2022. High-capacity compact massive MIMO array with hybrid decoupling scheme. *IEEE Trans Antenn Propag*, 70(10):9292-9304. https://doi.org/10.1109/TAP.2022.3184551

Lin HW, Chen QG, Ji Y, et al., 2020. Weak-field-based self-decoupling patch antennas. *IEEE Trans Antenn Propag*, 68(6):4208-4217. https://doi.org/10.1109/TAP.2020.2970109

Liu F, Guo JY, Zhao LY, et al., 2020. Dual-band metasurface-based decoupling method for two closely packed dual-band antennas. *IEEE Trans Antenn Propag*, 68(1):552-557. https://doi.org/10.1109/TAP.2019.2940316

Liu GY, Yang N, Leung KW, et al., 2024a. A full design perspective of port decoupling for MIMO antennas: preservation of radiation pattern. *IEEE Trans Antenn Propag*, 72(12):9164-9176. https://doi.org/10.1109/TAP.2024.3484680

Liu GY, Yang N, Leung KW, 2024b. Radiation pattern decoupled circular polarization microstrip antennas using metal pins. IEEE Int Workshop on Antenna Technology, p.98-100. https://doi.org/10.1109/iWAT57102.2024.10535819

Liu RP, An X, Zheng HX, et al., 2020. Neutralization line decoupling tri-band multiple-input multiple-output antenna design. *IEEE Access*, 8:27018-27026. https://doi.org/10.1109/ACCESS.2020.2971038

Ma LN, Shao ZJ, Lai J, et al., 2023. A compact dual-decoupling scheme for aperture-coupled and probe-fed closely spaced wideband microstrip antennas. *IEEE Trans Antenn Propag*, 71(11):9072-9077. https://doi.org/10.1109/TAP.2023.3306637

Madani S, Jog S, Lacruz JO, et al., 2021. Practical null steering in millimeter wave networks. Proc 18th USENIX Symp on Networked Systems Design and Implementation, p.903-921.

Mondal P, Dhara D, Harish AR, 2024. A partially reflective FSS-based superstrate as a decoupling structure for reducing the mutual coupling of circularly polarized antennas. *IEEE Trans Antenn Propag*, 72(4):3652-3661. https://doi.org/10.1109/TAP.2024.3364750

Odabasi H, Salimitorkamani M, Turan G, 2023. Mutual coupling reduction between closely placed patch antennas using complementary U-shaped polarization converter. *IEEE Antenn Wirel Propag Lett*, 22(11):2710-2714. https://doi.org/10.1109/LAWP.2023.3276527

Ozer S, Kouhalvandi L, Matekovits L, et al., 2024. Design of wideband metasurface structure with the aid of bottom-up optimization. Int Conf on Electromagnetics in Advanced Applications, p.316-319. https://doi.org/10.1109/ICEAA61917.2024.10701815

Paulraj AJ, Gore DA, Nabar RU, et al., 2004. An overview of MIMO communications—a key to gigabit wireless. *Proc IEEE*, 92(2):198-218. https://doi.org/10.1109/JPROC.2003.821915

Poli R, Kennedy J, Blackwell T, 2007. Particle swarm optimization: an overview. *Swarm Intell*, 1(1):33-57. https://doi.org/10.1007/s11721-007-0002-0

Qi XL, Peng MG, Zhang HM, et al., 2024. Anti-jamming hybrid beamforming design for millimeter-wave massive MIMO systems. *IEEE Trans Wirel Commun*, 23(8):9160-9172. https://doi.org/10.1109/TWC.2024.3359286

Qian JF, Izquierdo BS, Gao S, et al., 2024. A novel low-cost H-plane decoupling technique for two closely placed patch antennas using electric and magnetic coupling cancellation. *IEEE Trans Antenn Propag*, 72(5):3864-3873. https://doi.org/10.1109/TAP.2024.3376075

Shi J, Geng X, Yan SC, et al., 2022. An approach to achieving multiple mutual coupling nulls in MIMO stacked patch

antenna for decoupling bandwidth enhancement. *IEEE Trans Circ Syst II Exp Briefs*, 69(12):4809-4813. https://doi.org/10.1109/TCSII.2022.3196020

Sun LB, Li Y, Zhang ZJ, 2021. Decoupling between extremely closely spaced patch antennas by mode cancellation method. *IEEE Trans Antenn Propag*, 69(6):3074-3083. https://doi.org/10.1109/TAP.2020.3030922

Tong CW, Yang N, Leung KW, et al., 2022a. H-plane radiation pattern decoupled patch antennas with zero edge-to-edge spacing using three-pair vias. Proc TENCON IEEE Region 10 Conf, p.1-3. https://doi.org/10.1109/TENCON55691.2022.9977581

Tong CW, Yang N, Leung KW, et al., 2022b. Port and radiation pattern decoupling of dielectric resonator antennas. *IEEE Trans Antenn Propag*, 70(9):7713-7726. https://doi.org/10.1109/TAP.2022.3177547

Tong CW, Yang N, Leung KW, et al., 2024. Design of MIMO antennas with DRAs and a dual-function decoupling/radiating monopole antenna. *IEEE Trans Antenn Propag*, 72(5): 3874-3885. https://doi.org/10.1109/TAP.2024.3378836

Wang MN, Shao ZJ, Tang M, et al., 2024. Miniaturization and decoupling of wideband stacked patch antennas based on spoof surface plasmon polaritons. *IEEE Trans Antenn Propag*, 72(10):8076-8081. https://doi.org/10.1109/TAP.2024.3416680

Wang ZB, Tu ZH, Yuan ZF, et al., 2023. Decoupling and wide-angle scanning design of a millimeter-wave phased array using square-ring metasurface. *IEEE Antenn Wirel Propag Lett*, 22(8):1828-1832. https://doi.org/10.1109/LAWP.2023.3266266

Wu JB, Tong CW, Yang N, et al., 2023. Radiation pattern decoupled patch antennas based on TM_{01} and TM_{11} modes. *IEEE Antenn Wirel Propag Lett*, 22(11):2695-2699. https://doi.org/10.1109/LAWP.2023.3296353

Xia RL, Qu SW, Li PF, et al., 2015. An efficient decoupling feeding network for microstrip antenna array. *IEEE Antenn Wirel Propag Lett*, 14:871-874. https://doi.org/10.1109/LAWP.2014.2380786

Xiao ZQ, Chen SQ, Zeng Y, 2024. Simultaneous multi-beam sweeping for mmWave massive MIMO integrated sensing and communication. *IEEE Trans Veh Technol*, 73(6): 8141-8152. https://doi.org/10.1109/TVT.2024.3350714

Xiong B, Zhu YZ, Xu YX, et al., 2024. A novel millimeter-wave 2D wide-angle scanning phased array antenna based on decoupling surface. *IET Microw Antenn Propag*, 18(11): 810-818. https://doi.org/10.1049/mia2.12521

Xu JP, He XN, Deng TW, 2024. A self-decoupled MIMO patch array with consistent radiation patterns. *IEEE Trans Antenn Propag*, 72(12):8971-8979. https://doi.org/10.1109/TAP.2024.3410535

Zhai JH, Cao YF, Xue Q, et al., 2024. Cross-band decoupling method for dual-band aperture-shared antenna array using metasurfaces. *IEEE Trans Antenn Propag*, 72(2):2001-2006. https://doi.org/10.1109/TAP.2023.3344212

Zhang S, Pedersen GF, 2016. Mutual coupling reduction for UWB MIMO antennas with a wideband neutralization line. *IEEE Antenn Wirel Propag Lett*, 15:166-169. https://doi.org/10.1109/LAWP.2015.2435992

Zhao BS, Tang M, Zhang YP, et al., 2024. Wideband decoupling of zero edge spacing laminated resonator antenna array. *IEEE Trans Antenn Propag*, 72(8):6481-6490. https://doi.org/10.1109/TAP.2024.3418518